Subcontractor Report

Properties of Wide-Gap Chalcopyrite Semiconductors for Photovoltaic Applications

Final Report
8 July 1998–17 October 2001

A. Rockett
University of Illinois
Urbana, Illinois

Properties of Wide-Gap Chalcopyrite Semiconductors for Photovoltaic Applications

Final Report
8 July 1998–17 October 2001

A. Rockett
University of Illinois
Urbana, Illinois

NREL

National Renewable Energy Laboratory

NOTICE

This report was prepared as an account of work sponsored by an agency of the United States government. Neither the United States government nor any agency thereof, nor any of their employees, makes any warranty, express or implied, or assumes any legal liability or responsibility for the accuracy, completeness, or usefulness of any information, apparatus, product, or process disclosed, or represents that its use would not infringe privately owned rights. Reference herein to any specific commercial product, process, or service by trade name, trademark, manufacturer, or otherwise does not necessarily constitute or imply its endorsement, recommendation, or favoring by the United States government or any agency thereof. The views and opinions of authors expressed herein do not necessarily state or reflect those of the United States government or any agency thereof.

Available electronically at http://www.osti.gov/bridge

Available for a processing fee to U.S. Department of Energy
and its contractors, in paper, from:
      U.S. Department of Energy
      Office of Scientific and Technical Information
      P.O. Box 62
      Oak Ridge, TN 37831-0062
      phone: 865.576.8401
      fax: 865.576.5728
      email: reports@adonis.osti.gov

Available for sale to the public, in paper, from:
      U.S. Department of Commerce
      National Technical Information Service
      5285 Port Royal Road
      Springfield, VA 22161
      phone: 800.553.6847
      fax: 703.605.6900
      email: orders@ntis.fedworld.gov
      online ordering: http://www.ntis.gov/ordering.htm

Printed on paper containing at least 50% wastepaper, including 20% postconsumer waste

Table of Contents

List of Figures

List of Tables

Final Report
Contract DOE NREL XAK-8-17619-34

Properties of Wide-gap Chalcopyrite Semiconductors for Photovoltaic Applications

University of Illinois
Angus Rockett P.I.

PROJECT SUMMARY:

The objectives of this project were to obtain a fundamental understanding of wide-gap chalcopyrite semiconductors and photovoltaic devices. Information to be gathered included significant new fundamental materials data necessary for accurate modeling of single and tandem-junction devices, basic materials science of wider-gap chalcopyrite semiconductors to be used in next-generation devices, and practical information on the operation of devices incorporating these materials. Deposition used a hybrid sputtering and evaporation method shown previously to produce high-quality epitaxial layers of $Cu(In,Ga)Se_2$ (CIGS). Materials analysis was also provided to assist members of the National CIS Team of which, through this contract, we were a member. Solar cells produced from resulting single-crystal epitaxial layers in collaboration with various members of the CIS Team were used to determine the factors limiting performance of the devices based on analysis of the results.

SUMMARY OF ACCOMPLISHMENTS:

Early in this program as we were deciding how to adapt to changing budgets (see Level of Effort Section at the end of the document), NREL announced a new record solar cell performance with the observation that the material had been processed in such a way as to result in a (110) preferential surface orientation. Because epitaxial growth allows us to determine the surface orientation of our films specifically by choice of the substrate surface on which the film is grown, a major focus of the project concerned the nature of (110)-oriented CIGS films and the performance of solar cells produced therefrom. We begin this summary therefore with a description of the results for growth on (110) GaAs, which formed a basis for much of the work ultimately conducted under the program.

Study of (110)-oriented CIGS

The following description was published originally in the Proceedings of the IEEE Photovoltaic Specialists Conference in Anchorage Alaska in August 2000.

CIGS films were deposited using a hybrid sputtering and evaporation technique. "Epi-ready" (110), (001) and (111)B GaAs substrates were introduced into the growth chamber without pre-treatment. Prior to growth the native oxide was desorbed by heating to 610 °C for 10 minutes.
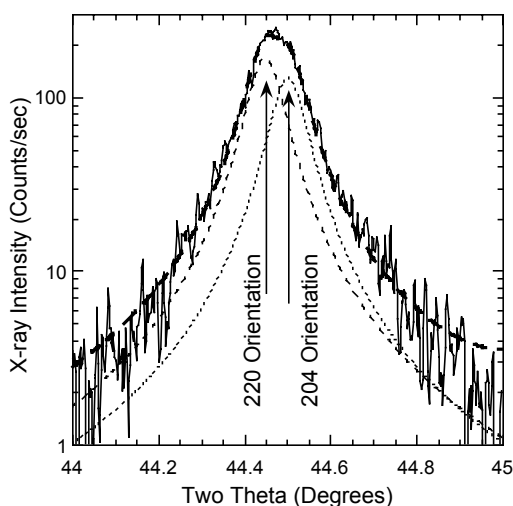
The In, Ga, Cu fluxes were generated by magnetron sputtering In and Cu-Ga alloy ($Cu_{0.72}Ga_{0.28}$ or $Cu_{0.8}Ga_{0.2}$) targets in 0.3 Pa ultrapure Ar gas. Se was supplied in excess from an effusion cell. The substrate temperature was measured by a thermocouple calibrated with optical pyrometry. The minimum temperatures for epitaxy were found to be 540, 640, and 700 °C for the (110), (100), and (111) substrates, respectively. Typical growth rates were 1.0 μm/hour and the thickness of grown layers ranged from 0.1 to 1.5 μm. After deposition, samples were cooled to 400 °C in 20–40 minutes under a reduced Se flux to prevent thermal expansion mismatch induced cracking. No Na was intentionally added to any of the films and Na levels in the epitaxial layers were low.

Surface morphologies were studied by scanning electron microscopy and atomic force microscopy. The thicknesses of the layers were measured by cross-sectional SEM. Average compositions were measured by energy dispersive X-ray spectroscopy (EDS) while depth profiles were obtained by secondary ion mass spectrometry (SIMS). The structure, orientation and crystal quality of the deposited layers were characterized by electron backscattering diffraction patterns (EBDP) and by X-ray diffraction (XRD) using a triple-axis high resolution diffractometer and Cu $K\alpha_1$ radiation. Typical resolution was 0.006° in 2θ. Electronic properties were measured by temperature-dependent Hall-effect and solar cell device fabrication.

Fig 1: An XRD scan of a CIGS layer on (110) GaAs. The peak includes two components corresponding to (220) and (204)-oriented domains.

Results and Discussion

Samples were grown over a wide range of compositions on all three substrates but concentrated on the near-stoichiometry slightly In-rich compositions typically used in high-performance solar cells. Films grown below ~600°C had Ga contents determined by the Cu-Ga target composition, while films grown at higher temperatures showed increasing Ga due to diffusion out of the substrates. A typical XRD scan from an epitaxial layer grown at 540°C on (110) GaAs is shown in Figure 1. Fitting the resulting spectrum showed two Lorentzian components centered at 44.452 and 44.508° with full widths at half maximum (FWHM) of 0.088° and 0.064°. The GaAs substrate peak FWHM was 0.0064°. Comparison with the standard powder diffraction data and the measured Ga composition of the film (Ga/In+Ga = 0.17) suggests that these two peaks correspond to approximately equal volume fractions of (220) and (204) domains. The small tetragonality of the unit cell at this composition makes domain boundaries common. The presence of the domains did not significantly disrupt the epitaxial growth but resulted in stacking

2

(a)

(b)
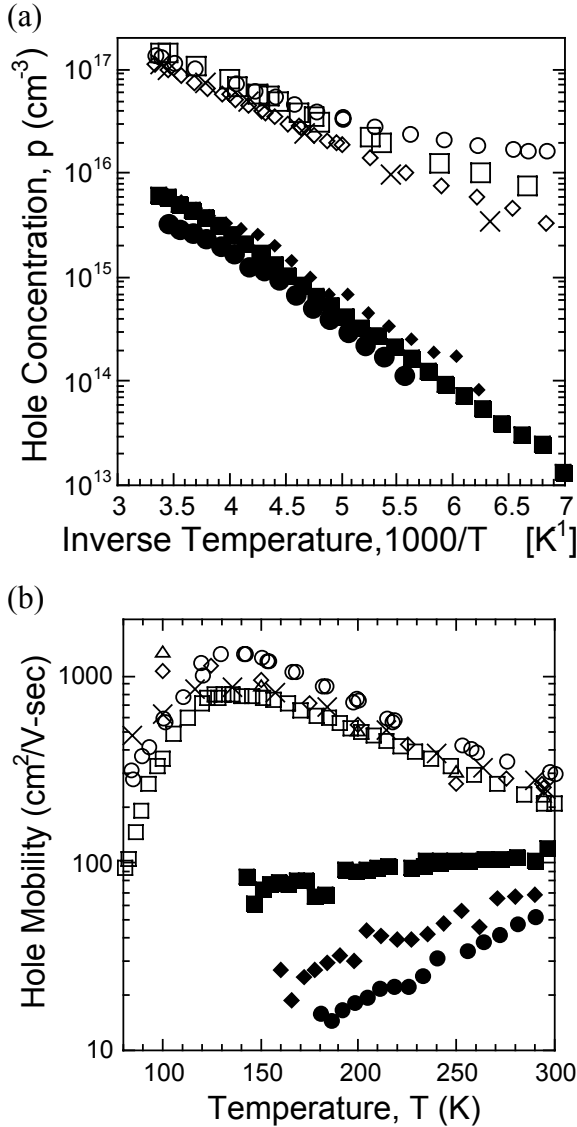
Figure 2: Shows the temperature dependence of (a) hole concentration and (b) mobility. Open points are for (112) samples, X indicates (002) results, and black filled points correspond to (220) samples.

faults. Such faults are common in most single crystal and polycrystalline CIGS as observed by several groups by transmission electron microscopy. Apparently the faults do not severely damage the performance of devices. However, we have found that they reduce cathodoluminescence efficiency and may be less common in higher performance materials. The latter is currently under investigation in ongoing research projects. The overall quality of the crystals was verified by EBDP, which showed single-crystal features over the entire surface of the films. For simplicity, in the remainder of the paper we will refer to the films as (220)-oriented, although the actual structure consists of rotated (220) and (204) domains.

The surface morphology of the (220) films shows a striking difference from (112) and (002) layers. (112) films had (112) surfaces with low pyramidal mounds. (002) surfaces had fine ripples along (110) directions leading to weak faceting toward [112]. Rectangular pits with (112) facets were also observed on the (002) films. By contrast, the (220) film surfaces broke up into (112) facet faces with equal amounts of each type [Se or metal terminated (112)]. Facet sizes increased with increasing growth temperature. Thus, the (220) surface consisted of large areas of opposite polarity facets. No evidence was found for (220) or (204) surface facets in spite of the (220) average film orientation.

Hole concentration and mobility for the (220) layers were determined as a function of temperature and the results are shown in Figure 2. A dramatically different behavior was found for the (220) samples compared to the behavior of the (112) and (002) samples. The hole concentrations are uniformly lower by a factor of ~20 in the (220) samples and the shallow acceptor present in the other samples is missing. In addition, the hole mobility is significantly reduced and changes its behavior. The extremely uniform nature of the mobilities in the (112) and (002) samples for all compositions contrasts with the large variability in the (220) samples. The mobility data can be interpreted as resulting from vertically-oriented defect clusters on (002) or (112) planes which intersect the current path of the Hall-effect measurement in the (220)

3

samples. If this is correct, then the lower mobility in the (220) samples may not be relevant to devices where carriers move normal to the film plane.

To understand the possible implications of the above results on device performances, the AMPS computer model was used to simulate hypothetical devices with varied hole concentrations. Uniform energy gap and graded-gap absorber devices were modeled and similar results were found with and without grading, although exact values of model parameters varied slightly. Typical values for materials constants were used for the CIGS, dip-coated CdS, and ZnO layers. The Mo back contact was assumed to produce a 0.3 eV Schottky barrier to p-CIGS. A back surface mirror of Ga-rich material was included but was only significant for non-graded devices. It was found that a thin (1-5 nm) n-type surface layer was essential to successful device simulations, as expected. The properties of the absorber layer (recombination cross sections and hole and defect concentrations) and the surface n-layer thickness and carrier concentration were adjusted to fit the record-performance solar cell current-voltage curve and spectral response. The blue response of the device was dominated by the CdS properties but a good fit was obtained with reasonable values for the dip-coated CdS material.

A good fit to the 18.8% NREL device performance on a (204)-oriented film was obtained with a hole concentration of $p=4x10^{15}$ cm^{-3} in the absorber layers, in agreement with typical values for high quality devices. Raising the carrier concentration in the model by 20x with no other changes in the model decreased the performance of the simulated device resulting in a good fit to the NREL device on (112) material (17.7% efficient). While this does not establish conclusively that the improvement in performance in the record device was due to the use of (220)-oriented films, it is suggestive.

Standard understanding of devices indicates that performance should improve with higher rather than lower carrier concentrations. This behavior was found in some simulations when the absorber had very high defect concentrations. However, an adequate simulation of both spectral response and current/voltage curve of the record device was not obtained when such high defect densities or cross-sections were used. Overall, the results above suggest that in a very high performance solar cell, a decrease in hole concentration of the magnitude observed in the epitaxial growth experiments could lead to the level of improvement obtained in devices at NREL.

Direct proof of improved performances with (110) oriented films was not obtained by fabrication of solar cells from the epitaxial layers. Best device performances ranged from 8.5% on a (112) epilayer to 6.4% on a device on a (220) layer. The relatively low performances most likely result from the relatively high Ga content (Ga/In+Ga ~0.3), the lack of intentionally-added Na, delays due to shipping the samples between growth and device fabrication, and the relative thinness of the epitaxial layers (0.75 μm). (Thick epitaxial layers [>1 μm] often crack.) The GaAs substrate may also have affected performances. Results for the devices on each orientation of epitaxial layer are given in Table I.

We conclude that the improved solar cell result reported for (204)-oriented CIGS was probably not the result of formation of (204) or (220) surfaces. This work shows those surfaces to be unstable and to decompose into (112) type facet faces during vapor phase growth. The lower

4

carrier concentration observed in (220)-oriented epitaxial layers could explain the improved device results based on simulations of the high performance device using AMPS. Epitaxial devices do not show this effect as the device performances are not sufficient to improve upon reduction in hole concentration in the absorber.

Table I: Solar Cell Results Summary Based on Epitaxial CIGS Layers

Solar cell performances in general are highest for layers on (111) substrates, followed by devices on (100) and finally on (110) layers. Open circuit voltages were highest on (100) layers. Variation in devices are significant and no clear conclusion can yet be drawn. We have modeled these results and concluded that the lower mobility of carriers in layers on (110) oriented surfaces is more damaging than the benefits expected from the lower carrier concentration.

Sample	Cell	eff (%)	ff (%)	Voc (mV)	Jsc (mA/cm^2)	Roc (Ω-cm^2)	Gsc (mS/cm^2)	Substrate Orientation	Ga/(In+Ga)
U.III-T58	1	8.5	58	465	31.6	3	3	111	
U.III-T58	2	4.1	48	277	31.0	3	17	111	
U.III-T58	3	7.7	57	418	31.9	3	4	111	
U.III-T58	4	7.7	57	418	32.3	3	2	111	
U.III-T58	5	8.2	60	422	32.4	2	3	111	
U.III-T58	6	7.7	57	413	32.6	2	3	111	
U.III-T157	2	1.2	23	358	14.2	37	38	100	0.21
U.III-T160	2	5.3	38	535	26.3	13	3	100	0.42
U.III-T59	1	4.4	45	392	24.6	6	12	100	0.19
U.III-T59	2	4.7	51	399	23.3	5	5	100	0.19
UIII.T35	5	6.6	57	455	25.5	3	3	100	
UIII.T35	4	6.7	59	462	24.6	3	2	100	
UIII.T35	3	7.3	61	483	24.8	3	2	100	
UIII.T35	1	1.1	25	508	8.6	59	17	100	
UIII.T35	2	5.4	63	514	16.7	5	1	100	
U.III-T132	1	5.3	45	403	29.1	4	11	110	0.37
U.III-T152	1	6.4	55	420	27.7	3	4	110	0.28
U.III-T153	1	3.7	47	378	20.7	5	14	110	0.40
U.III-T155	1	5.3	50	405	26.1	4	9	110	0.31
U.III-T161	1	2.3	40	309	18.6	6	23	110	0.52

Surface Morphology of (110)-oriented CIGS Films

Figure 3: XRD spectra of CIGS (110) epitaxial layers.

Even though there is not an obvious correlation between film orientation and device performance, the surface growth mode was of considerable interest and greatly clarifies the nature of the growth process. The observations reported by our group for growth of epitaxial layers on GaAs (110) are in substantial agreement with the morphology of polycrystals with a (110) preferred orientation grown at NREL for the record device performances.

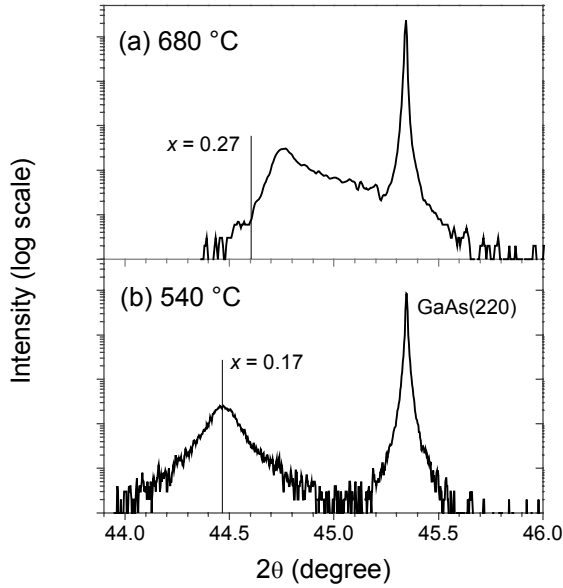The following description was published recently in the Journal of Applied Physics:

Conditions for (220)/(204) Epitaxial Growth

Using the hybrid sputtering and evaporation method, epitaxial layers with a range of compositions were obtained by varying the flux ratio of Cu-Ga relative to In and by changing the Cu-to-Ga ratio in the Cu/Ga target. Cu contents were adjusted by controlling the In target current (and hence flux) relative to the Cu-Ga target current. Cu/(In+Ga) ratios in the films ranged from 0.82 to 0.93. The films were near stoichiometry with $\Delta s=(2[Se]/([Cu]+3([In]+[Ga]))-1$ smaller than 0.06 but always positive (excess Se). These are also the compositions used for absorber layers of high-efficiency solar cells.

Epitaxy was demonstrated by EBSD. For epitaxial layers on GaAs (001) and (110) substrates, consistent EBSPs were collected across the whole sample area and all observed Kikuchi bands matched perfectly with those from the respective GaAs substrates, indicating that epitaxial layers were obtained. For layers on GaAs(111)B, two alternating sets of patterns were obtained: one matching those of the substrate, the other corresponding to twins that rotated the crystal lattice 180° about the substrate normal. Most films grown under Cu-poor conditions have a high density of stacking faults and twins. Our layers on GaAs(111)B show about 40% of the surveyed areas having rotated backscattering patterns and a typical twinned domain size of 2-4 µm. The patterns from all epitaxial layers were more diffuse than those from the GaAs substrates and fewer Kikuchi bands were resolved.

In principle, it is possible to determine the orientation of a chalcopyrite crystal by identifying the diffraction symmetries of certain zone axes in EBSPs. For example, the [001] axis in the chalcopyrite structure is a tetrad with Laue space group 2mm, the same as the <100> axes in the sphalerite structure, while the [010] and [100] axes are Laue space group 2 and, therefore, have
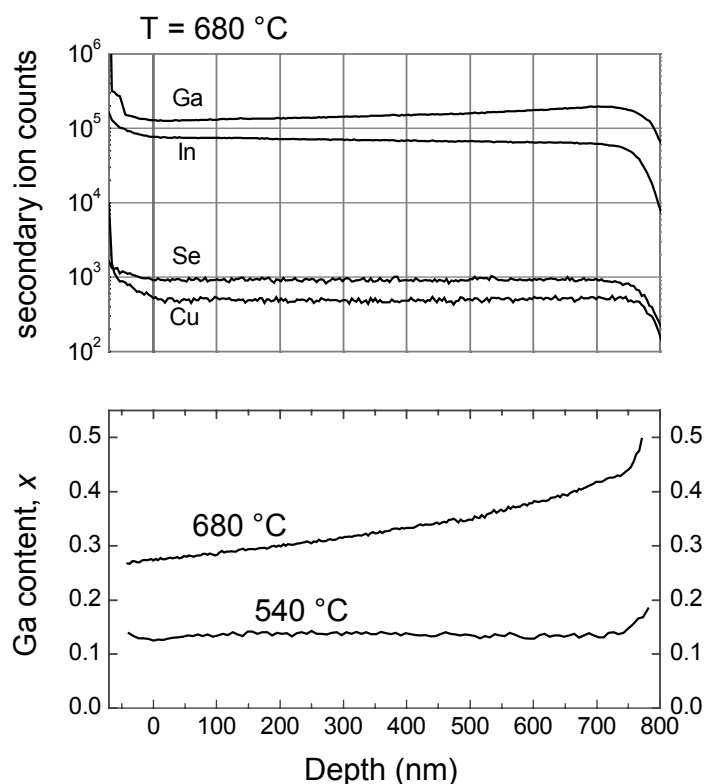
6

Figure 4. SIMS depth profiles of CIGS epitaxial layers on (110) GaAs

no mirror planes. In practice, however, it is very difficult to identify any asymmetrical features because CIGS of the composition studied here is approximately isometric ($c/2a \sim 1$). We were not able to identify any of those asymmetrical features unique to chalcopyrite. Possible explanations include the limited dynamical range of the CCD camera, surface roughness, multiple unit-cell orientation domains, and other defects in the films.

Standard ("$\omega/2\theta$") XRD scans show only substrate and CIGS peaks. No polycrystallinity or peaks from minority second phases were observed. Fig. 3 shows the spectra of two CIGS/GaAs(110) epitaxial layers grown under different conditions. Sample (a) $CuIn_{0.73}Ga_{0.37}Se_{2.18}$ (average composition measured by EDS) was grown at 680 $^{\circ}$C with the $Cu_{0.72}Ga_{0.28}$ target. Its composition depth profile is shown in Fig. 4 and its surface morphology in Fig. 5. Sample (b) $CuIn_{0.95}Ga_{0.16}Se_{2.27}$ was grown at 540 $^{\circ}$C with the $Cu_{0.8}Ga_{0.2}$ target. The thickness of both layers is about 750 nm. The shapes of the peaks were strongly influenced by Ga diffusion from the substrate. The full width at half-maximum (FWHM) of the primary CIGS (220)/(204) peaks, estimated from fitting the spectra with mixed Gaussian-Lorentzian curves, were 0.10° and 0.12° for samples (a) and (b) respectively.

The peak fit for the sample deposited at 540°C is shown in Fig. 1. While the peak is relatively broad, it includes a flattened top indicating the presence of multiple constituents. We know the Ga content of the film from the EDS, the XRD peak position, and the SIMS analysis. Thus, we can estimate the relative positions of the (220) and (204) peaks. The best fit to the peak shows the presence of both (220) and (204) reflections, although the data does not permit reliable relative intensity determinations. It does appear though that both domains are present in the material in roughly equal quantities.

Figure 5: Surface morphology of (110) epitaxial layers. (a) High temperature, (b) low temperature

The tetragonal chalcopyrite structure of CIGS is closely related to the sphalerite structure of the substrate. A CIGS unit cell can be derived from two cubic unit cells of ZnSe by orderly substitution of the Zn atoms with Cu and In atoms. The resulting unit cell does not have a height (c) of twice the base dimension (a) because Cu-Se and In-Se have different bond lengths. However, because the Ga-Se bond length differs from that of In-Se, the c/a ratio is a function of $x = Ga/(In+Ga)$ ratio, progressing from $c/a > 2$ for $x = 0$ to $c/a < 2$ for $x = 1$. It is clear that when the CIGS is grown epitaxially on sphalerite substrates, multiple orientations are possible depending on the alignment of the c-axis with respect to the substrate. Generally, the preferred orientation is such that the strain energy due to lattice mismatch is minimized, although exceptions exist. Growth kinetics and surface energy variations were proposed as possible causes of the exceptions. For our CIGS layers, the c/2a ratios are very close to unity, thus the difference in strain energy due to orientation variation is minimal and multiple orientations most likely coexist in the layers.

8

Rocking curve peak FWHM values from 0.41° to 0.51° were found for the CIGS/GaAs (110) layers. This is much larger than typical values of ~0.2° for the epitaxial CIGS on GaAs (001) or (111)B, indicating a distinctly larger range of tilt angles between domains in the crystal structure and thus presumably more dislocations.

Different epitaxial temperatures were found for substrates of different orientations: 540°C for (110), 640 °C for (001), and 700 °C for (111)B. Below these temperatures, the layers were polycrystalline. The process of epitaxy requires accommodation of each type of atom at its proper location on the lattice by insertion into surface steps. We note that the differences in epitaxial temperature correlate well with the differences in density of steps on the respective surfaces. Thus, on the (111)B substrates, the surface would be expected to consist almost entirely of Se-terminated facets, with metal-terminated facets only present upon rare inclined faces or on surface steps. On (001) substrates the surface consists of highly-elongated ripples which emphasize the $(112)_{Se}$ termination but which include significant amounts of both types of step. On (110) surfaces the average surface is composed of exactly equal numbers of both types of exposed surface (metal and Se) intermixed on a relatively fine scale. Thus, any type of adatom should be straightforward to accommodate with relatively short diffusion distances. As expected, we find that the epitaxial temperature is apparently correlated with an effective distance needed for a given atom to reach an acceptable growth step.

Ga Diffusion in (220)/(204) Oriented Films

The temperature dependence of the Ga diffusivity is apparent from the shapes of the XRD peaks. Samples grown at 680°C showed broad (220)/(204) XRD peaks (Fig 3), corresponding to a change of lattice constant with the change of Ga content through the depth of the films. On the other hand, samples grown at 540°C have well-defined symmetric peaks (Fig 3). SIMS analysis of the (220)/(204)-oriented films showed that little interdiffusion occurred at low temperatures (~ 540 °C) but increased at higher temperatures (Fig. 4). At 680 °C, the [Ga]/([Ga]+[In]) ratio, x, rises from about 0.27 near the surface to 0.45 near the CIGS/GaAs interface, while the Cu, Ga+In and Se contents remain approximately constant throughout the film. Similar Ga diffusion results were obtained for other orientations, although lower deposition temperatures were not possible due to the higher epitaxial temperatures.

A large lattice mismatch is expected between the CIGS and the GaAs. Typical mismatch strains would be ~1.2% to 1.6% based on the Ga contents and growth temperatures used in this study with a corresponding critical thicknesses for strain relief of ~20 nm. Strain energy reduction thus provides a significant driving force for diffusion of Ga into the epitaxial layer during growth as observed previously for other substrate orientations. However, the films suffer tensile thermal stresses during the post-growth cooling because the thermal expansion coefficient of the CIGS is larger than that of the substrate ($\alpha_{CIS}=11.0\times10^{-6}$ K^{-1}, $\alpha_{GaAs}=6.96\times10^{-6}$ K^{-1}). In cases where thick layers (> 750 nm) were allowed to cool rapidly after growth, cracks were observed along [001] directions due to this mismatch strain. Cracking was much more common for films grown on (110) GaAs than other orientations, presumably because of either the asymmetry of the (220)/(204) surface or because of higher resolved stress on the fracture planes.
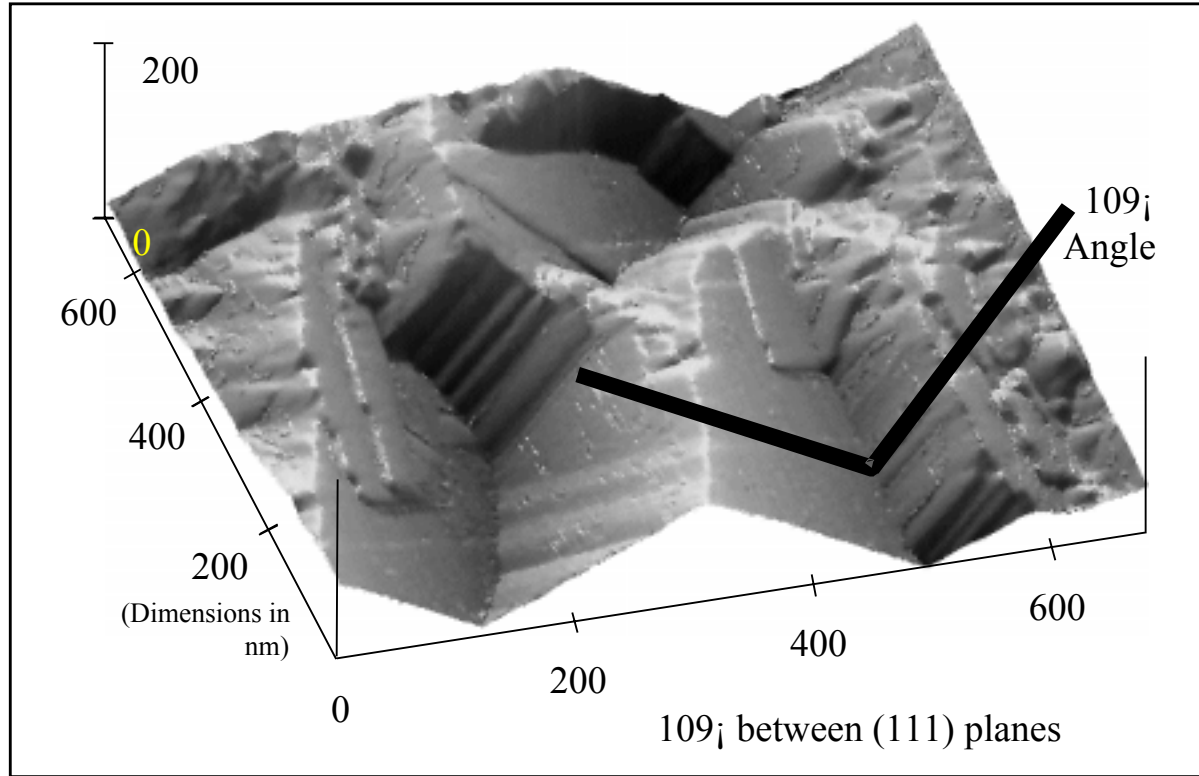
Figure 6: Shows a surface region of a (110)-oriented Cu(In$_{0.7}$Ga$_{0.3}$)Se$_2$ epitaxial layer. Although representative, the majority of the facet faces are smaller those in the figure. Facet sizes increase with film thickness. Note that the two faces are separated by the angle between (112) planes, as expected, and that one family of planes is far smoother than the other.

Surface Morphology of CIGS (220)/(204)

Fig. 5 shows the SEM images of two epitaxial films grown at (a) 680°C and (b) 540°C, and discussed above. Both surfaces are replete with facets. Apparently, the surface morphology depends strongly on the growth temperature. Sample (a) exhibits large, extended and well-defined facets in contrast to the much smaller features on sample (b). However, close inspection reveals that all films share two major facet types parallel to [1$\bar{1}$0] directions and oblique with respect to the substrate normal. One set of planes tilts toward [002]/[100], and the other tilts toward [00$\bar{2}$]/[$\bar{1}$00]. We will call these planes types A (the larger, flatter facets) and B (smaller, rougher facets), respectively (see Fig 6 for their cross section profiles). Type A facets are atomically flat (112) planes extended in the [$\bar{1}$10] direction, having widths in the [002]/[100] directions from ~10 to ~500nm. B-type facets are heavily stepped, consisting of ($\bar{1}$12)-orientated faces and [012] and [102]-orientated steps. In transition regions where different facets meet, the step height and density increases sharply and in many cases small vertical ($\bar{1}$12) and (1$\bar{1}$2) facets exist.

10

Low temperature films exhibit the same types of facets but with smaller faces. The type-A facets are especially small and discontinuous in the [$\bar{1}$10] direction and are inclined ~26° with respect to the substrate surface. Type B facets are relatively wide with a curved contour and a less steep angle of about 17° with respect to the substrate due to their multiple surface steps. Small vertical facets were also observable. The major effect of increased growth temperature seems to be on the facet size and orientation.

The surface morphology observed suggests a three-dimensional behavior in which terrace nucleation and terrace growth compete to control surface morphology. It is hypothesized that growth on the surface of type B facets is much faster than on type A facets and that the films grow through nucleation of new layers on top of the type B facets. This accounts for the surface morphology and the relative tilts of surface planes shown in Fig. 6. At elevated temperatures the terrace width on type B facets increases as a result of the higher mobility of surface species. The concurrent reduction in free adatoms on the surface will simultaneously reduce step nucleation. Note that the {112} A and B type facets are polar with one consisting of a mixture of Cu, Ga, and In atoms while the other consists of Se atoms.

Absolute polarity identification is possible by special diffraction techniques, among which X-ray anomalous dispersion method and Kossel experiments are most widely used. In practice, calibrated chemical etching is more convenient and frequently used instead. Unfortunately, in the case of Cu(In,Ga)Se$_2$, no report about the preferential etching properties is available. However, if we assume that the bonding at the epitaxial growth interface is Ga to Se or As to Cu, Ga, or In, the epitaxial layer must maintain the polar orientation of the substrate, i.e., the polarity of the surface can be deduced from that of the substrate. It has been established that (111)A is the slowest etching direction in GaAs under certain etchants. The polar orientation can be readily determined by examining the preferential etching profiles with an optical microscope. The results here show that type A facets have a {112}Me surface and type B facets a {112} Se surface.

Summary

XRD confirms the formation of epitaxial layers and a distinct mosaic structure on GaAs (110). Ga diffuses through the films at higher growth temperatures as was observed previously for other CIGS epitaxial layer orientations. Pronounced faceting was observed on the surfaces of the films. The epitaxial temperature for the (220)/(204) layers is considerably lower than that on any other surface tested and is attributed to the higher density of both types of surface steps. The surface is proposed to grow by motion of Se-terminated terraces across Se-terminated surface facets, causing these facets to be rough and leaving the metal-terminated facets relatively smooth. The facet growth rate is moderate relative to the rate of nucleation of new facets.

Modeling of Solar Cell Device Performances

Modeling of solar cells was carried out using the AMPS computer code. The majority of the following results were obtained under the current program, although the final analysis was

conducted under follow-on programs in the High Performance PV and Beyond the Horizons programs.

MODEL

Solar cell simulations presented here used the AMPS computer code developed at the Pennsylvania State University by S. Fonash et.al. This code uses the Newton-Raphson method to solve the Poisson and two continuity equations. AMPS requires a large amount of input data for the active layers as well as the reflectivity, work function, and recombination rates at the top and bottom contacts. AMPS produces a wide-variety of outputs, including current-voltage curves, spectral response, carrier generation and recombination rates as a function of depth, and others. It is necessary to use as many of these results as possible in determining the adequacy of the fits.

Selection of AMPS Input Parameters

The first step in modeling any solar cell is to obtain a detailed analysis of its performance. While capacitance/voltage and deep level analyses would be helpful, the minimum necessary set includes light and dark current-density/voltage (j/V) and bias-dependent spectral response. Temperature-dependent j/V measurements are very helpful in removing contact behaviors from the results as well. For this work, device results were provided by the Institute for Energy Conversion at the University of Delaware (IEC), Global Solar Energy (GSE) and Shell [Siemens] Solar (SS).

Given this data to fit, the second step is to obtain a composition depth profile from which the absorber layer composition [x and y in $Cu(In_xGa_{1-x})(S_ySe_{1-y})_2$] can be determined. (See Figure 7) Based on values of x and y, the conduction and valence band edges can be approximated. Here composition depth profiles were obtained by SIMS. The energy gap was assumed to be given by $E_{gap} = 0.95 + 0.8x - 0.17x(1-x) + 0.7y - 0.05y(1-y)$. The valence band offset was taken as 20% of the
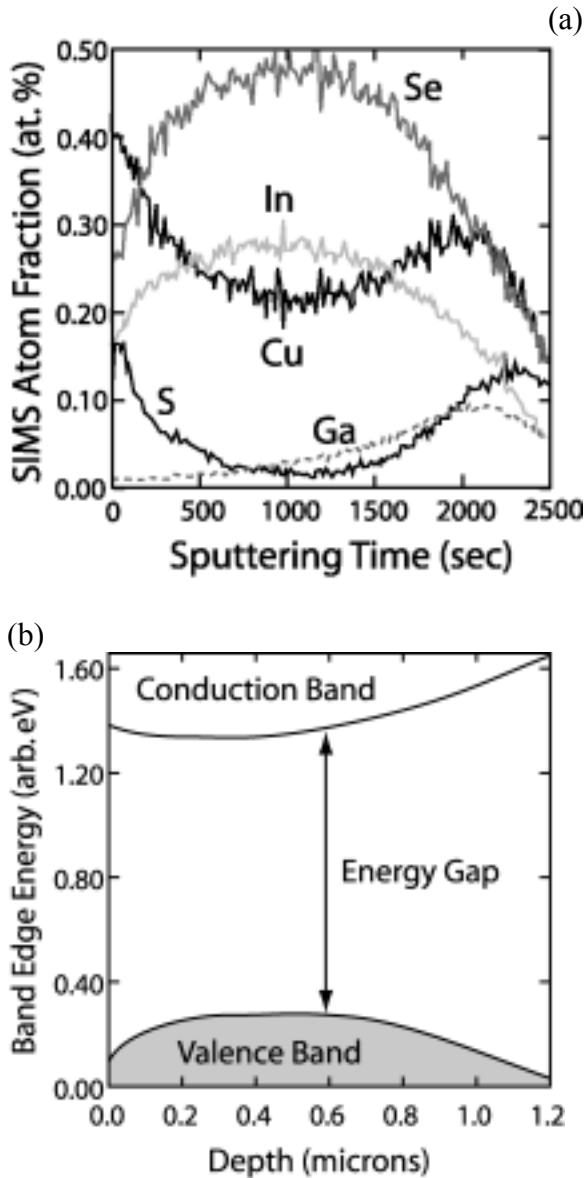

Figure 7. Shows (a) the results of a SIMS profile of a SS device, and (b) the corresponding energy band edges as a function of depth.
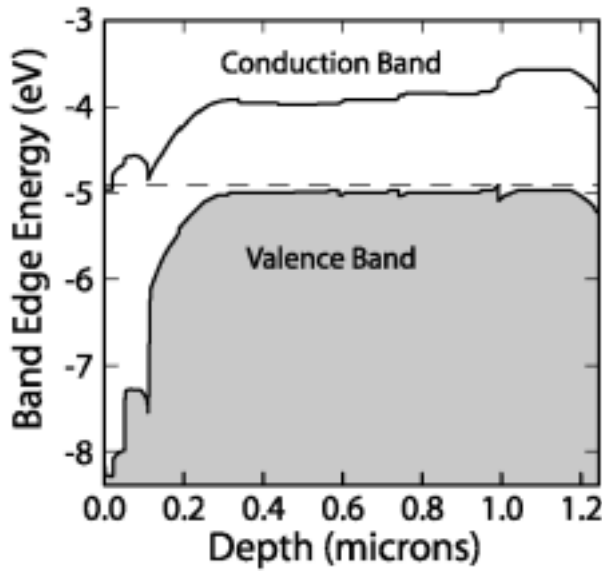
12

Figure 8: A band edge diagram resulting from the AMPS computer code.

change in gap due to x and 80% of the change in gap due to y. While very rough estimates, these values are probably good enough considering the other assumptions made when entering data into AMPS. An example of a composition depth profile for a SS absorber and the corresponding estimated band edges are given in Fig. 8. This was then converted into discrete segments manually and entered into AMPS. Absorption coefficients were taken from published data for $CuInSe_2$ and shifted to account for changes in energy gap. CdS absorption was based roughly on published data but net results varied significantly from laboratory to laboratory based on spectral response curves. This is due primarily to thickness differences in the CdS layers but also somewhat to changes in composition resulting from different dip-coating recipes.

The primary input parameters used here for AMPS are given in Table II. In addition, there are parameters for the front and back contacts and the ZnO layers. For the front contact, the work function is relatively unimportant as long as it does not contribute series resistance. Top contact reflectivity was used to fit the peak spectral response, was between 0.1 and 0.05, and was constant for a given device laboratory. Back contact reflectivities were fit based on the red response edge for the cell. In general, adequately sharp red-response edges were not obtained unless the reflectivity of the back contact was between 0.5 and 1.0. The back contact work function should be 0.75 eV based on literature values for Mo. This resulted in excessively high Schottky barriers in graded-junction devices rich in Ga to the rear of the device. A temperature-dependent characterization of a SS device showed a light-dependent Schottky barrier with a fixed height of ~0.3 eV but where the reverse saturation current was light-dependent. Because the SS device is relatively thin, it is likely that light penetrated to and affected the rear contact. The observed barrier height does not correspond well to the Mo work function and the assumed band edge positions. Here, the barriers were reduced by increasing the Mo work function. The true barrier is either very leaky due to high doping at the back contact or to interfacial defects or the electron affinity of the CIGS is lower than assumed in this work. Finally, the recombination velocities for both contacts were set to the AMPS default of 10^7 cm/sec, roughly the thermal velocity of carriers.

The properties of the ZnO layer were largely irrelevant to the fits with the exception of avoiding a large band-offset with the CdS and avoiding excessive absorption. The ZnO was assumed to have an electron affinity of 4.00 eV with an energy gap of 3.30 eV. The donor concentration in the n^{++} ZnO was assumed to be 10^{20} cm^{-3}. Moderate variations in these estimated values did not have a significant effect on the simulations. Because the minority carriers have all recombined

13

with majority carriers within the ZnO, trapping and transport rates are not very important to the results.

TABLE II

Primary Band Properties	Source	Values from	CdS Values	Interlayer	CIGS Values
Energy Gap	Estimate	Data	2,4-2.8	1.25 eV	0.95-1.7 eV
Electron Affinity	Estimate	Literature, Fit	3.80	3.95	4.00-3.80 eV
Dielectric Const	Known	Literature	10	13.6	13.6
Conduct Band DOS	Estimate	Literature	10^{19} cm^{-3}	10^{19} cm^{-3}	10^{19} cm^{-3}
Valence band DOS	Estimate	Literature	10^{19} cm^{-3}	10^{19} cm^{-3}	10^{19} cm^{-3}
Electron Mobility	Data	Data	0.1 cm^2/Vs	8 cm^2/Vs	8 cm^2/Vs
Hole Mobility	Data	Data	0.1 cm^2/Vs	8 cm^2/Vs	8 cm^2/Vs
Discrete Defects					
1° Defect Density	Known	Literature range	6×10^{12} cm^{-3} *	$\leq 2\times10^{21}$ cm^{-3}	10^{16}-10^{17} cm^{-3}
Ionization Energy	Known	Literature range	none	0.04 eV	0.04-1.35 eV
Defect band width	Estimate		none	0.04 eV	0.01
Electron cross section	Fit	10^{-12}-10^{-18} cm^{-2}	none	1.4×10^{-14} cm^{-3}	1.4×10^{-14} cm^{-3}
Hole cross section	Fit	10^{-12}-10^{-18} cm^{-2}	none	1.4×10^{-14} cm^{-3}	1.4×10^{-14} cm^{-3}
Gaussian Defects					
Hole trap 1 density	Data	J. Heath & D. Cohen	1×10^{14} cm^{-3} *	10^{14} cm^{-3}	10^{14} cm^{-3}
Trap 1 depth	Data	J. Heath & D. Cohen	1.20 *	0.80	0.80
Trap 1 width	Data	J. Heath & D. Cohen	0.10 *	0.13	0.13
Electron cross section	Fit	10^{-12}-10^{-18} cm^{-2}	10^{-14} cm^{-3} *	2×10^{-14} cm^{-3} *	2×10^{-14} cm^{-3} *
Hole cross section	Fit	10^{-12}-10^{-18} cm^{-2}	10^{-14} cm^{-3} *	2×10^{-14} cm^{-3} *	2×10^{-14} cm^{-3} *
Hole trap 2 density	Data	J. Heath & D. Cohen	none	10^{15} cm^{-3}	10^{15} cm^{-3}
Trap 2 depth	Data	J. Heath & D. Cohen		1.00	1.00
Trap 2 width	Data	J. Heath & D. Cohen		0.13	0.13
Electron cross section	Fit	10^{-12}-10^{-18} cm^{-2}		2×10^{-14} cm^{-3} *	2×10^{-14} cm^{-3} *
Hole cross section	Fit	10^{-12}-10^{-18} cm^{-2}		2×10^{-14} cm^{-3} *	2×10^{-14} cm^{-3} *
Band Tail Properties					
Band tail slope	Data	J. Heath & D. Cohen	0.05 eV *	0.022	0.022
Density of tail states	Data	J. Heath & D. Cohen	2×10^{20} cm^{-3} *	10^{18} cm^{-3}	10^{18} cm^{-3}
Electron cross section	Fit	10^{-12}-10^{-18} cm^{-2}	10^{-15} cm^{-3} *	10^{-14} cm^{-3}	10^{-14} cm^{-3}
Hole cross section	Fit	10^{-12}-10^{-18} cm^{-2}	10^{-15} cm^{-3} *	10^{-14} cm^{-3}	10^{-14} cm^{-3}
* Indicates a fit value. These values had little impact on the fit results for the values shown. All cross section values were kept constant for a given defect but the values were adjusted to fit the IEC cell					

The most important input parameters are those for the CIGS and CdS. These include absorption coefficient (measurable), energy gap and electron affinity (estimated as described above), dielectric constant and band edge density of states (from AMPS defaults), and carrier mobilities and gap states (fit as restricted by literature values). When values were not known, such as defect cross sections for interactions with free carriers, these parameters were adjusted to fit an IEC device with no compositional gradients. Resulting values are listed in Table II. The relatively low values of electron and hole mobilities were based on recent Hall-effect measurements of p-CIGS similar to that used in the absorbers of devices simulated here. Higher values up to those measured for single crystals (~300 cm^2/V-sec at 300 K) are possible for carriers traveling within individual grains. Nominally, electron mobilities should be higher than hole mobilities. Modeling shows some effect of the mobilities but the effect is very weak.

The primary relatively *unknown* variables that are critical to device models are the defect and doping states in the CIGS and CdS. Trapping and release rates are important, and doping levels are significant to establishing depletion widths. Preliminary experimental data are now available

for some of the devices modeled here concerning deep level densities and energies in CIGS. The interesting feature of these results is that they are consistent for a wide range of Ga contents and deposition techniques. Important to using AMPS is data on tails on the CIGS bands and trap states near the conduction band edge. The results suggest that the wider band tail has a characteristic width of ~0.022 eV. A reasonable source of such band tails is compositional disorder on the metal sublattice including both antisite and vacancy defects. Such defects are commonly thought to accommodate stoichiometry variations in the material. Furthermore, alloying generally replaces Ga with In. Overall, it seems likely that defects would primarily broaden the conduction band edge. In current fits, both edges were broadened symmetrically for lack of specific data for the sharper edge.

The experimental data also yielded evidence of trap states 0.8 eV and 1.0 eV above the valence band edge with concentrations and miniband widths as shown in Table II. Experimentally-observed densities of these states were assumed for the fit of the IEC device. From this fit, cross-sections were determined. The same defects were assumed to also be present in the GSE and SS materials and to have the same interaction cross-sections. Only the band tail widths, the concentration of defects and the band tail energies were allowed to change from device fit to device fit. The acceptor concentration in device layers ranges from 0.8 to 20 x10^{16} cm^{-3}. Various studies have characterized these values and fits were forced to stay within this range.

Finally, it should be noted that the surface of the CIGS must be inverted (n-type). Here this was accomplished by the addition of the thinnest possible n-type interlayer (2 nm) with properties as listed in Table II.

RESULTS

The j/V and QE data for an IEC device of constant composition were fit to determine the defect cross-sections for given defects as listed in Table II. The true figure of merit is probably the product of cross section and defect density. Based on fitting of the relatively simple IEC structure, two graded-composition devices, one from GSE containing only a Ga gradient, and one from SS containing both a Ga and S gradient were fit. It provides some confidence in the values in Table II, that changing only the band edges, defect concentrations, and the back Schottky barrier, good fits to all devices could be obtained. SIMS analysis results (Fig 7) for an SS device led to the AMPS band edges shown in Fig 8. A similar band-edge diagram (without S effects) was obtained for the GSE device. Parameter values in AMPS were not changed as a function of alloy composition, although the defect density is likely to rise in high Ga-content alloys. Note: it is not claimed here that the fits reported are definitive, and only aspects of the fits which appear relatively unequivocal are discussed below. Thus issues such as changes in defects with composition could be included but can only be treated in an ad-hoc way at this point.

More significant conclusions from AMPS

Very strong inversion of the CIGS/CdS interface is essential to fitting the device results here. The simulation suggests a carrier concentration of the order of >10^{21} cm^{-3} in the interlayer, corresponding to roughly one dopant state in 50 atoms. This would be reasonable for donor

defects driven by an interfacial layer. Such a high (or even higher) concentration of donors is nearly essential to understanding the interface given the possibility of Fermi level pinning by point defect cluster decomposition in an n-type region.

Given what is known about the defect states and band tails, the most sigificant remaining fitting parameter is the acceptor density of states in the absorber. Because this determines the depletion width and affects recombination and carrier concentations, it has a large effect on the results. Satisfactory fits were obtained within the expected concentration range with little change from one material to another. Better data on acceptor density would be important to improving fits. In addition, hole and electron mobilities had a modest effect. Electron mobility primarily affects the blue portion of the spectral response, while the hole mobility primarily affects the red response. Surprisingly, increasing the carrier mobility can decrease the spectral response and short-circuit current in some simulations.

Based on the experimental data shown in Fig 7 and the SS AMPS fits (Fig 8), it appears that for expected values of acceptor density in this material the sulfur penetrated too far into the device, resulting in a bump in the conduction band edge. This bump, while not large, probably resulted in a loss of red-response in the device. Such red-response degradation was exacerbated by low carrier mobilities.

All of the devices modeled here showed significant light-to-dark crossover in the j/V curves. Such photoconductivity is normally thought to result from defects in the CdS. No satisfactory light-to-dark crossover was obtained by introducing defects in the CdS simulated layer. These defects only led to series resistance in the device. However, the CIGS/CdS conduction band offset and the CIGS band tail widths both affected light-dark crossover. A systematic experimental study of band tail effects on crossover would be helpful. Higher CIGS/CdS band offsets produced more photoconductive response but reduced fill factor due to series resistance. The photoconductive effect due to the band offset was limited and adequate fits of experiments were not obtained. Probably the majority of the disagreement concerning cross-over is in inadequate parameters or in problems with the model of the CdS.

Surface Morphology and Growth Mode of CIGS (112)

Toward the end of the contract period, we began a study of the difference in surface morphology and surface properties of the two surfaces (112)A and (112)B which were observed for the growth on (110) GaAs. Because substrates can be prepared with the (111) A and B surfaces, these two surfaces can be grown independently. The work, reported at the IEEE Photovoltaic Specialists Conference in New Orleans in 2002 was begun under the current program. The following results were obtained during the final quarter of this program.

EXPERIMENTAL

CIGS films were deposited using a hybrid sputtering and evaporation technique. Commercially supplied ``epi-ready'' (111)B and (111)A GaAs wafers were used as substrates. The In, Ga, and Cu fluxes are generated by magnetron sputtering of In and Cu or Cu-Ga alloy targets in 99.9999 % pure Ar at a pressure of 0.3 Pa. Se is supplied in excess from an effusion cell. Layers with a

range of compositions were obtained by varying the flux ratio of Cu-Ga relative to In and by changing the Cu-to-Ga ratio in the Cu-Ga target. Growth temperatures ranged from 480 to 720 °C. Typical growth rates were 1 μm/hr and the thicknesses of grown layers were 0.1-1.5 μm. After deposition, samples were cooled slowly to 400 °C in 20--40 minutes under a reduced Se flux to reduce film-substrate interface decohesion and film cracking. Decohesion problems limited the thickness of most films to ~0.75 μm, which was found to reliably avoid such decohesion problems. This probably limits the performance of solar cells produced from these layers.

Epitaxial CIGS films with compositions typical of the absorber layers of the high-efficiency solar cells were deposited. The [Cu]/([In]+[Ga]) ratios ranged from 0.82 to 0.93 and were near stoichiometry. Epitaxy was demonstrated by electron backscattering and x-ray diffraction. Consistent electron backscatter patterns were collected across sample surfaces and all observed Kikuchi bands matched perfectly with those from the respective GaAs substrates, indicating that epitaxial layers were obtained. XRD spectra show only substrate and CIGS peaks. No extra peaks from polycrystalline grains or minority second phases were observed. The epitaxial temperature was ~540 °C for growth on GaAs (110), ~640 °C on GaAs (001), ~660 °C on GaAs (111)A, and ~700 °C on GaAs(111)B.

The resulting films were characterized extensively by atomic force microscopy (AFM), scanning electron microscopy (SEM), electron backscattering diffraction (EBSD) analysis, X-ray diffraction (XRD), secondary ion mass spectrometry (SIMS), Auger electron spectroscopy (AES), and angle-resolved photoelectron spectroscopy (XPS). Solar cells have also been produced from these layers by W. Shafarman at the Institute for Energy Conversion at the University of Delaware and have been further characterized by J. Heath and D. Cohen at the University of Oregon and by Y. Strzhemechny and L. Brillson at the Ohio State University, and scientists at the National Center for Photovoltaics at NREL. The AFM instrument has a vertical resolution sufficient to resolve fractions of surface step heights, with lateral resolutions of ~1 nm on some surfaces.

RESULTS

Films on (110) GaAs spontaneously facet to polar (112) faces of two opposite polarities, as described above. To further analyze the two polar surfaces in detail, samples were grown on polar (111) GaAs surfaces. The films are assumed to take the polarity of the underlying substrate. Both of the resulting surfaces have remarkably similar surface morphologies, consisting of wide, atomically-flat, and remarkably triangular surface terraces forming broad triangular pyramids on the surfaces, see Fig 9. The pyramids on both surfaces have a shallow facet angle of up to 2° and are typically several microns on a side. The Se-terminated $(112)_B$ films contain 180° rotational twins, leading to similar rotations of the pyramids. This is easily observable in SEM and AFM micrographs of the surfaces. Metal-terminated $(112)_A$ surfaces show no twinned regions. Backscatter pattern analyses show a small tilt angle between adjacent pyramids. In spite of the differences in twinning, the films morphologies are remarkably similar, especially in light of the differences observed on the (110)-oriented films. This is not surprising in one respect. The morphology on the (110) films is determined by transfer of atoms from one polar surface to the other with growth dominated by one face. On the polar (112) surfaces, no
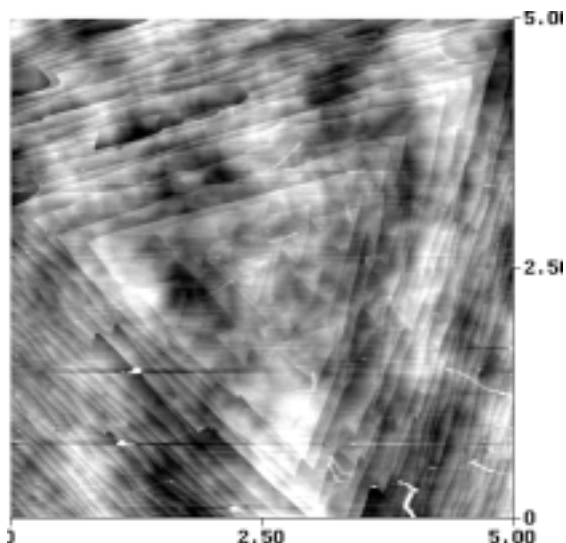
Figure 9: An AFM image of the surface of a (112)$_A$-oriented CIGS surface. The steps shown are single atomic height or a few bilayers per step.

such transfer is possible and both are constrained to grow at a rate determined by the atomic fluxes.

Small terraces on thin films are almost always round or only partially faceted. On the CIGS films the terraces are extremely triangular. There are six possible surface step orientations of two types. One type has single dangling bonds while the other has two dangling bonds per atom in the step edges. Analysis of the morphology of the (110)-oriented films when combined with the structure of the (112) polar facets suggests that the two-dangling-bond-per-atom step geometry dominates these surfaces. One would expect that such steps would have higher energies than the single-dangling-bond steps unless there is a regular organization of the steps or a step-edge reconstruction. We anticipate that such a reorganization can easily occur given the alternation of atoms on the steps. One of the three steps of each type has alternating metal atoms (Cu-In-Cu-In in CuInSe$_2$), while the other two types have pairs of atoms of one kind followed by pairs of the other kind (Cu-Cu-In-In along the step edge). The extreme preference of the surface steps for one geometry is remarkable and almost unknown among compound surfaces.

Cathodoluminescence Depth Profiling

The near surface behavior of CIS epitaxial layers is clearly interesting based on the above work. To investigate this behavior further, we conducted a collaborative research program with L. Brillson and Y. Strzhemechny. The results were reported in the Journal of Vacuum Science and Technology.

EXPERIMENTAL

Two types of samples were investigated. Specimens of the first type with a free CIGS surface had chalcopyrite epilayers grown on GaAs wafers by a hybrid sputtering and evaporation technique from Cu, Cu-Ga and In magnetron sources and a Se effusion cell as described above. All the CIGS single-crystals yielded good-quality rocking curves. The CIGS layers had approximately the same thickness of 750 nm for all orientations. Average compositions for each sample were determined by energy dispersive spectroscopy. All the samples were group-III rich and had a *p*-type bulk conductivity. The hole concentration for those sample varied within 10^{-16} - 10^{-17} cm^{-3} with the Hall mobilities ~300 cm^2/V-sec at room temperature. The present choice of the Ga/(In+Ga) ratios corresponds to the relative abundances found to produce record cell efficiencies. The samples of the second type studied - polycrystalline CIGS surfaces, in a

18

CdS/CIGS heterojunction as well as free surfaces - were prepared at the National Renewable Energy Laboratory using multisource evaporation. The structure consists of a molybdenum covered soda-lime glass substrate, over which a ~2 μm thick polycrystalline CIGS layer, followed by a 60 nm CdS layer are deposited.

The cathodoluminescence spectroscopy (CLS) experiments were performed in a UHV chamber equipped with a cold stage. An electron beam of variable energy and flux was electronically chopped to improve signal detection. A Carl Leiss single flint prism monochromator dispersed the CL intensity for spectral analysis. Liquid nitrogen cooled Ge and thermoelectrically cooled S-20 detectors and a Stanford Research lock-in amplifier detected the CL emissions.

RESULTS

CIGS/GaAs epilayers

CIGS epilayers deposited on GaAs substrates exhibit strong differences in surface morphology as a function of growth orientation. In agreement with previous measurements as part of the investigations described above, the (112) samples are covered with smooth pyramids spaced roughly 5 μm apart and ~80 nm high. The (002) surfaces appear to be flat terraces 0.5-1.0 μm wide separated by 100-200 nm troughs. Elongated pit-and-furrow ripples can be observed,
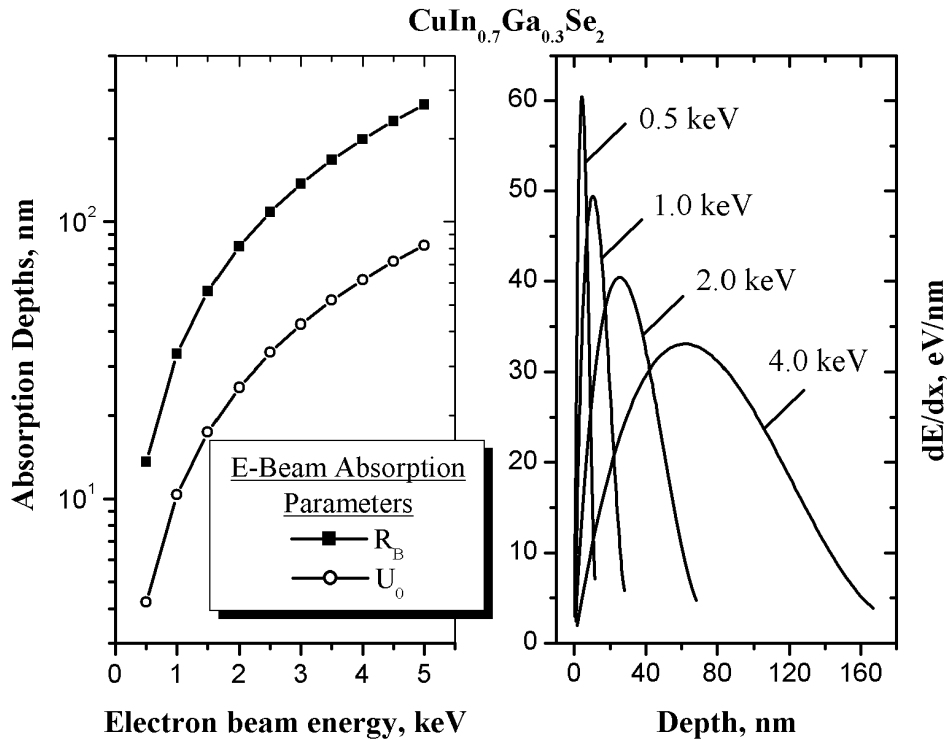

Figure 10: Predicted electron beam absorption depths for a series of primary electron beam energies.

associated with the (112) polar planes. The (220)/(204) surfaces exhibit rough ledges 100 nm high, spaced 150 nm apart. The two polar {112} facets, selenium- or metal-terminated, produce these ledges on the (220)/(204) faces. As can be seen from these AFM images, the (112) surface is the smoothest and the (220)/(204) surface is the roughest. The SEM images (not shown) are in good agreement with the AFM results.

It would be quite natural to assume that these distinctions in surface morphology may bring in differences of the types of planar and point defects present, and variations in their depth distribution. In order to determine whether these variations in surface morphology lead to differences in electronic defects, we use a low energy, depth-resolved form of CLS, termed Low Energy Electron Nanoluminescence (LEEN) Spectroscopy, as the primary tool to probe the optoelectronic properties of the surface and their variations with depth. The LEEN technique is based on the energy dependence of excitation depth with electron beam energy increasing on a keV scale. Figure 10 shows the quantitative relationship between the electron beam energy E_B, the maximum range of penetration R_B, and the depth of maximum electron-hole pair creation U_0 for the nucleon and density values of $CuIn_{0.7}Ga_{0.3}Se_2$. Similar curves apply to other In/Ga ratios. Figure 11a illustrates the major LEEN results for the (112) orientation. Here, two major peaks are evident − a near-band edge (NBE) emission and a deep level (DL) feature. These major spectral features are similar for the other orientations. This similarity is remarkable, considering the substantial differences in surface morphology.
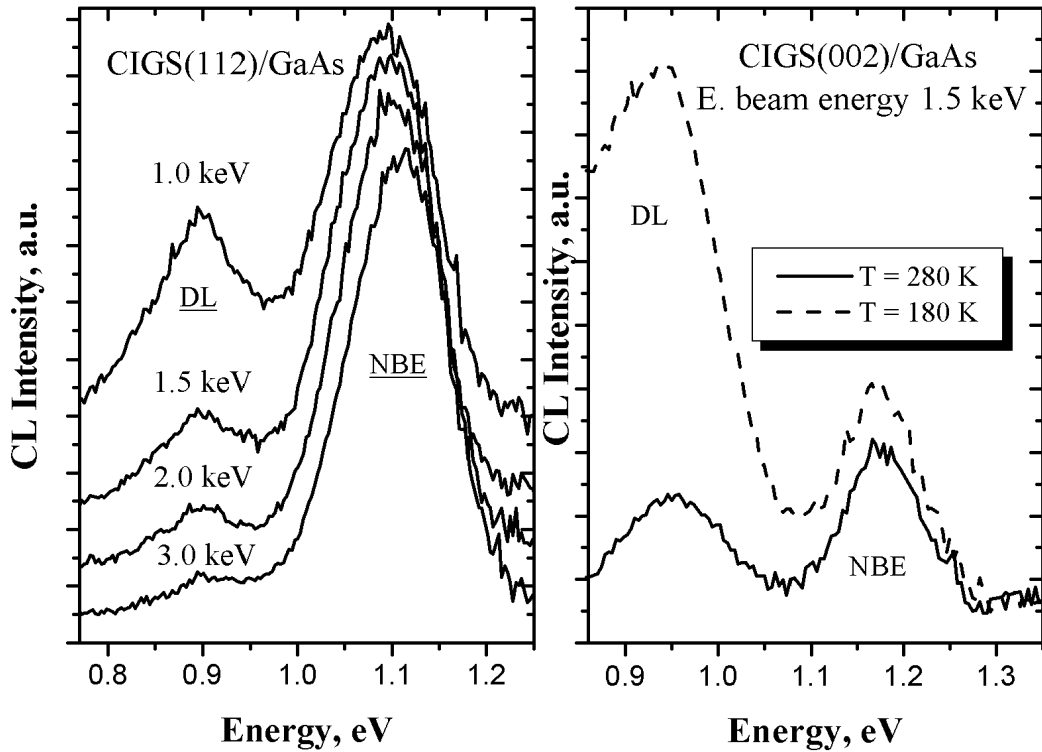

Figure 11: Cathodoluminescence results for (a) single-crystal epitaxial layers [LEFT] and (b) polycrystalline material from NREL [RIGHT].

LEEN experiments were also run with the sample stage cooled down to 180 K. Figure 11b shows a typical temperature variation of the CL spectra demonstrating an increased DL emission intensity at lower temperatures. These measurements are evidence for different thermal quenching behaviors of the DL and the NBE peaks.

Perhaps the most important aspect of Fig. 11a is that the DL intensity relative to the CIGS NBE emission intensity decreases with increasing depth of excitation. This behavior is observed for all CIGS orientations, regardless of surface morphology. Fig. 12 shows the DL/NBE ratio as a function of electron beam energy E_B. The decrease in I(DL)/I(NBE) with increasing E_B indicates that deep level emission resides preferentially in a surface and sub-surface layer less than a hundred nm thick. Error bars are associated primarily with a slow, time-dependent decrease in the NBE emission with electron beam exposure and, to a lesser extent, with slight sample-to-sample variations. DL emission intensity does not change with beam exposure. The decrease in the relative DL vs. NBE signal with increasing excitation depth is a very strong indication that, despite modest differences in composition and significant differences in surface morphology, we observe a systematic behavior in all our samples: formation of a surface layer with altered electronic properties tens of nanometers thick with relatively strong DL signal.
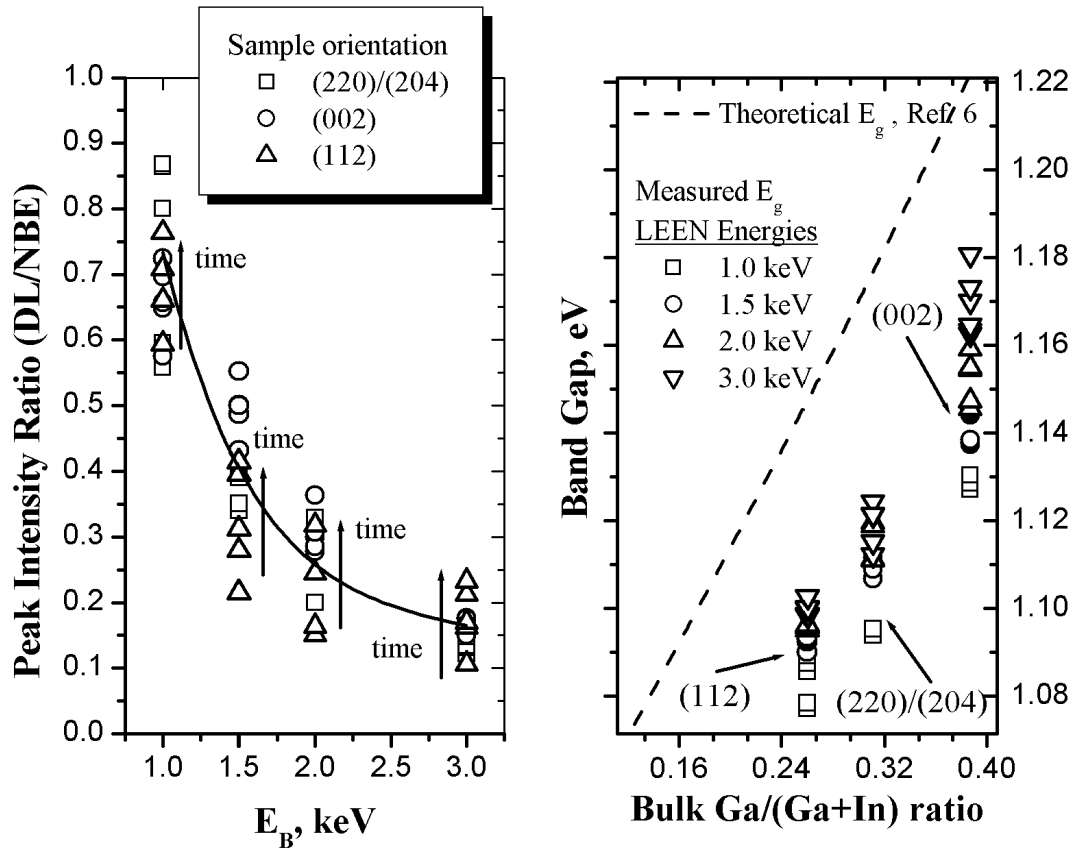

Figure 12: **CL intensity data as a function of beam energy and film composition. Film composition values were based on EDS measurements.**
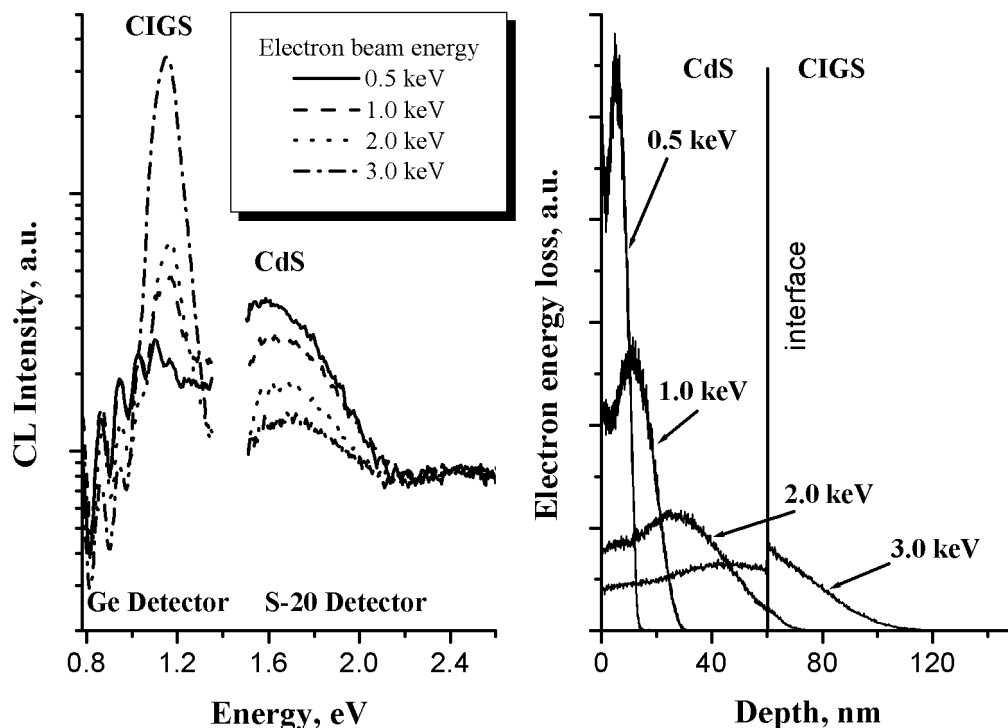
Figure 13: CL intensity results and depth simulations for the polycrystalline device layers obtained from NREL.

The measured NBE energies for all the samples agree with those expected based on the specimen stoichiometries. The NBE energy for the (220)/(204) orientation (not shown) is ~ 1.12 eV, and for the (002) orientation, it is ~ 1.16 eV. Since the value of the CIGS band gap energy is sensitive to the Ga to group III ratio, this NBE energy is expected to vary for the different orientations. The values of the NBE emission energies and hence the values of the band-gap measured by LEEN are in excellent agreement with the predicted values based on the bulk stoichiometry.

Polycrystalline (CdS)/CIGS/Mo/Glass (heterojunction) films

We also applied LEEN analysis to investigate electronic properties at the polycrystalline CIGS surface, free and in a heterojunction, specifically, a solar cell prototype. An AFM image (not shown here) of the top surface of this (solar cell) structure reveals roughness comparable to that of the epilayers. Irregular formations hundreds of nm high and with sub-micron-to-micron lateral features dominate the surface, apparently reflecting similar roughness of the underlying CIGS layer interface. The thickness of the CdS layer (~ 60 nm) makes it well suited for probing with LEEN since the interface is easily distinguished from CdS surface features at energies that retain nanoscale localization. The main features of this depth analysis for the heterojunction sample appear in Fig. 13. They are: CdS broad DL band at 1.6-1.7 eV, CIGS near NBE emission at 1.15 eV with multiple peaks below. Figure 13 shows that the strong DL emission in CdS decays with depth relative to the growing CIGS NBE emission. (For these low E_B, the DL

22

emission of the CIGS itself is almost absent.) Multiple peaks are observed in the low-energy range of the spectrum. They can be explained by the cavity resonance interference and will be discussed below.

Monte-Carlo calculations provide the LEEN energy-range relationship in Figure 13 and indicate the distribution of excited electron-hole pairs within the *p-n* junction geometry. Fig. 13 indicates that excitation of the buried CIGS layer is not expected to have a significant spectral contribution until E_B exceeds 1.5 keV. This is in agreement with the intensity behavior in Fig. 13 and is an indicator of the nanoscale diffusion length of minority carriers that would otherwise eliminate the pronounced dependence on excitation depth.

LEEN spectral features of a free polycrystalline CIGS surface (not shown) are similar to those in Figure 13: a pronounced NBE luminescence together with lower energy interference fringes. Naturally, the broad higher-energy emission associated with the deep levels of CdS is not observed.

DISCUSSION

In CIGS, the properties of the surface strongly depend on the bulk stoichiometry. CIGS-based solar cells employ In/Ga-rich chalopyrite layers with Cu/(In+Ga) ratio similar to the one in the current studies. Our Auger measurements reveal a Cu-deficient surface composition, consistent with device simulations (see above). The LEEN-based observations described above suggest that we may observe a unique surface chemistry in the CIGS/GaAs epilayers. Figures 11 and 12 explicitly demonstrate that there is a nanometer scale layer with relatively high defect emissions. This phenomenon is apparently insensitive to the crystal growth orientation and the surface morphology associated with it. Sample-to-sample bulk composition deviations have no significant effect as well, despite the fact that even slight variations of the Cu/In ratio may notably affect the positions of the emission peaks for In-rich materials.

It should be noted that the strong dependence of surface morphology on crystal orientation is not unexpected. This phenomenon results from the discrepancies in surface stability in different crystallographic directions. The most stable surface facets are formed by one of the two (112) surfaces, either Se or metal terminated. This high stability of the (112) planes leads to termination of mostly all surfaces (for different growth orientations) with those polar facets and explains the observed differences in surface morphologies. It is reasonable to assume that a high near-surface concentration of uncompensated defects causes the DL peak. Formation of a large number of electrically neutral defect complexes such as (V_{Cu}^{-1} In/Ga_{Cu}^{2+} V_{Cu}^{-1}) is expected to produce such low a density of holes. The probability of formation as well as the self-arrangement of these complexes can be significantly affected by the proximity of the surface. Since the surface layer is believed to have an inverted, *n*-type conductivity the surface concentration of donors should exceed the bulk values. Although thermally quenched relative to emission at low temperature (see Figure 12b), the DL emission is observed even at room temperature and is likely to be related to a free-to-bound transition rather than a donor-acceptor pair. The latter transitions are observed in photoluminescence spectra at lower temperatures and reveal their bound-to-bound characteristic behavior. Our temperature-dependent and excitation intensity-dependent photoluminescence studies are more consistent with bound-to-free interpretation and

will be published elsewhere. The origin of a deep donor defect, separated by ~200 meV from the bottom of the conduction band, is not well established. Nonetheless, a reasonable assignment can be made, based on previous theoretical predictions. An alternative to this picture can also explain the dependencies in Figs. 11 and 12. One can speculate that the relatively lower efficiency of the NBE radiative recombination is due to a higher surface concentration of non-radiative recombination centers. However, such non-radiative recombination would be expected to decrease all features in the spectra as is commonly observed in other systems.

In the case of CdS/CIGS interface (Fig. 13), we observe similar variations of deep level vs. NBE emission intensities with the depth of excitation. Here, the deep level-related emission is localized in a thin CdS overlayer. The nature of this DL emission is commonly associated with sulfur vacancies. Moreover, the intensity of this emission seems to be stronger at the CdS free surface. At the same time, in contrast to Fig. 11, the DL of CIGS is (tremendously reduced and is) obscured by the low-energy multiple-peak emission. There is qualitative and quantitative evidence that the latter could be explained by a resonance on the CIGS optical cavity of the radiation excited in the sample. Positions of the fringes are consistent with interference maxima on a cavity with a dielectric constant of 2.8 and a measured thickness of 2.5 μm. Occurrence of this resonance phenomenon in the Mo/glass-based samples may be related to specific reflective properties of the CIGS/Mo interface. It is quite natural to assume, that the origin of the fringes is in the broad deep-level emission extending into the band gap. Analysis of the LEEN spectra for the polycrystalline CIGS not capped with CdS indicates that the relative integrated intensity of this deep-level radiation exhibits a depth dependence similar to that shown in Fig 13 for the CIGS/GaAs epilayers. This is another substantiation of a distinct surface phase. Numerical analysis and discussion of these results will be published elsewhere. Comparison of the LEEN spectra for the polycrystalline CIGS with and without a CdS overlayer suggests that the CdS/CIGS heterojunction does not yield any radiative transitions associated specifically with the interface states and the band offsets. (The absence of any detectable CIGS DL emission may be due to a passivation of the near-CIGS-surface region by the CdS capping.) However, one should be cautious in comparing the LEEN results obtained on epitaxial CIGS/GaAs vs. polycrystalline CdS/CIGS/Mo/glass samples. The sample preparation was based on different growth techniques and might have produced significant structural and compositional differences. In this respect, it would be appropriate to perform systematic LEEN studies of the CdS/CIGS interfaces employing CIGS single-crystal epilayers.

The depth dependence of the CIGS emission intensity spectra in Fig.13 can also provide an estimate of the diffusion length of minority carriers within the CdS overlayer. The Monte Carlo simulations provide the expected range of excitation, whereas the LEEN spectra indicate the range of excitation plus diffusion of minority carriers. Hence, at the E_B for which LEEN spectra show the exponential onset of CIGS NBE emission, the difference between these two lengths yields the diffusion length. For the CdS/CIGS sample studied here, the CdS thickness of ~ 60 nm minus the ~ 20 nm excitation depth interpolated to occur at ~ 1.0 keV, yields a diffusion length of holes within the CdS overlayer of ~ 40 nm.

SUMMARY

CIGS epilayers grown with different orientations and similar chemical compositions on GaAs substrates exhibit large differences in surface morphology. Nevertheless, these CIGS epilayers reveal similar surface and sub-surface electronic properties, namely the formation of a top layer tens of nanometers thick with the deep level emission rising at the free surface. CIGS band gap energies measured are consistent with predictions for the specific stoichiometries investigated. The CIGS deep level energy is consistent with formation of In/Ga-rich antisite-vacancy pairs. In a prototype CdS/CIGS heterointerface, we observe a broad resonating DL emission in the CIGS along with a defect emission in the overlayer CdS. In addition, depth dependent LEEN gives a measure of a minority carrier diffusion length in the CdS nanoscale overlayer.

Other Activities in Support of the CIS National Team:

The Principal Investigator participated regularly in the CIS National Team Meetings throughout the period of the contract and provided microanalysis of samples from various laboratories, including Shell Solar, Global Solar Industries, Energy Photovoltaics, International Solar Electric Technologies, Unisun, and others.

In addition to these activities, A. Rockett was invited to chair a team on $Cu(In,Ga)Se_2$ at the Basic Resarch Opportunities in Photovoltaics meeting in Seattle. The team prepared a report on basic research opportunities in CIGS which was published in the Proceedings of the Electrochemical Society. A. Rockett presented an invited overview of the Basic Research Opportunities in Photovoltaics workshop held in May of 1999 in Seattle at the NCPV Program Review.

Publications and Other Output Under This Program:

1. Rockett, K. Granath, S. Asher, M.M. Al. Jassim, F. Hasoon, R. Matson, B. Basol, V. Kapur, J.S. Britt, T. Gillespie, and C. Marshall, "Na Incorporation in Mo and $CuInSe_2$ from Production Processes", Solar Energy Materials and Solar Cells **59(3)**, pp 255-264 (1999).

2. M. Bodegard, K. Granath, L. Stolt, and A. Rockett, "The Behavior of Na Implanted into Mo Thin Films During Annealing", Solar Energy Materials and Solar Cells **58(2)**, 199 (1999).

3. A.Rockett, "The Electronic Effects of Point Defects in $Cu(In_xGa_{1-x})Se_2$ Devices", AIP Conf. Proc. **462** 132 (1999).

4. A. Rockett, R.N. Bhattacharya, C. Eberspacher, V. Kapur, and S.-H. Wei, "Basic Research Opportunities in Cu-Chalcopyrite Photovoltaics", in *Photovoltaics for the 21st Century*, ed. by V.K. Kapur, R.D. McConnell, D. Carlson, G.P. Ceasar, and A. Rohatgi, proceedings volume 99-11 (The Electrochemical Society, Pennington, NJ, 1999).

5. D. Liao and A. Rockett, (220)-Oriented Cu(In,Ga)Se$_2$ -- Evidence that it may improve solar cell performance", Proc. 28th IEEE Photovoltaic Specialists Conf., Anchorage AK, Sept 15-22, 2000 (Institute of Electrical and Electronics Engineers, New York, 2000), 446-9.

6. M. Bodegard, O. Lundberg, J. Kessler, A. Rockett, and L. Stolt, "High Voltage Cu(In,Ga)Se$_2$ Devices with Ga-Profiling Fabricated Using Co-Evaporation", Proc. 28th IEEE Photovoltaic Specialists Conf., Anchorage AK, Sept 15-22, 2000 (Institute of Electrical and Electronics Engineers, New York, 2000), pp.450-3.

7. A. Rockett, "The Electronic Effects of Point Defects in CuIn$_{1-x}$Ga$_x$Se$_2$", Thin Solid Films **361-2**, 330-7 (2000).

8. A. Rockett, J.S. Britt, T. Gillespie, C. Marshall, M.M. Al Jassim, F. Hasoon, R. Matson, B. Basol, "Na in selenized Cu(In,Ga)Se$_2$ on Na-containing and Na-free glasses: distribution, grain structure, and device performances." Thin Solid Films **372(1-2),** 212-217 (2000 Aug 22).

9. D. Liao and A. Rockett, "EFFECT OF SURFACE ORIENTATION ON THE GROWTH AND PROPERTIES OF Cu(In,Ga)Se$_2$", Proc. 29th IEEE Photovoltaic Specialists Conf., New Orleans, LA, May 20-24, 2002 (Institute of Electrical and Electronics Engineers, New York, 2002).

10. A. Rockett, "PERFORMANCE-LIMITATIONS IN Cu(In,Ga)Se$_2$-BASED HETEROJUNCTION SOLAR CELLS", Proc. 29th IEEE Photovoltaic Specialists Conf., New Orleans, LA, May 20-24, 2002 (Institute of Electrical and Electronics Engineers, New York, 2002).

11. D. Liao and A. Rockett, "Epitaxial growth of Cu(In,Ga)Se$_2$ on GaAs(110)", J Appl. Phys **91**(4), 1978-83 (2002).

12. Y.M. Strzhemechny, P.E. Smith, S.T. Bradley, D.X. Liao, A.A. Rockett, K. Ramanathan, and L.J. Brillson, "Near-surface electronic defects and morphology of CuIn$_{1-x}$Ga$_x$Se$_2$", Journal of Vacuum Science & Technology B, vol.20, no.6, Nov. 2002, pp.2441-8.

LEVEL OF EFFORT:

This program was originally planned as a large effort to examine wide-gap materials, jointly funded by NREL and the Electric Power Research Institute (EPRI). Because of changes in funds availability at EPRI, their contribution was substantially reduced. The tasks and deliverables were reduced accordingly. Through careful control of spending, a significant amount was accomplished in the end. The funding ran from 7/16/98 through 10/31/01. The funding by year was as follows: 1998: $16,000 from NREL, $32,000 from EPRI (carried over from a prior contract); 1999: $40,750 from NREL, $74,000 from EPRI (partially carried over); 2000: $45,350 from NREL, $45,000 from EPRI; 2001: 37,400 from NREL, no support from EPRI. The program supported Dongxiang Liao, a graduate student, who performed all of the work except

the modeling of solar cells. A second student, Shawn O'Conner was also supported briefly. Solar cells were fabricated and tested at the University of Delaware Institute for Energy Conversion by Dr. William Shafarman and coworkers based on epitaxial layers supplied by the University of Illinois and at Uppsala University by A. Rockett in collaboration with K. Granath and L. Stolt.

REPORT DOCUMENTATION PAGE

Public reporting burden for this collection of information is estimated to average 1 hour per response, including the time for reviewing instructions, searching existing data sources, gathering and maintaining the data needed, and completing and reviewing the collection of information. Send comments regarding this burden estimate or any other aspect of this collection of information, including suggestions for reducing this burden, to Washington Headquarters Services, Directorate for Information Operations and Reports, 1215 Jefferson Davis Highway, Suite 1204, Arlington, VA 22202-4302, and to the Office of Management and Budget, Paperwork Reduction Project (0704-0188), Washington, DC 20503.

1. AGENCY USE ONLY (Leave blank)	2. REPORT DATE July 2003	3. REPORT TYPE AND DATES COVERED Final Subcontractor Report 8 July 1998–17 October 2001

4. TITLE AND SUBTITLE
Properties of Wide-Gap Chalcopyrite Semiconductors for Photovoltaic Applications: Final Report, 8 July 1998–17 October 2001

6. AUTHOR(S)
A. Rockett

5. FUNDING NUMBERS
PVP35001
XAK-8-17619-34

7. PERFORMING ORGANIZATION NAME(S) AND ADDRESS(ES)
University of Illinois
1-107 ESB, MC-233
1101 W. Springfield Ave.
Urbana, IL 61801

8. PERFORMING ORGANIZATION REPORT NUMBER

9. SPONSORING/MONITORING AGENCY NAME(S) AND ADDRESS(ES)
National Renewable Energy Laboratory
1617 Cole Blvd.
Golden, CO 80401-3393

10. SPONSORING/MONITORING AGENCY REPORT NUMBER
NREL/SR-520-34335

11. SUPPLEMENTARY NOTES
NREL Technical Monitor: B. von Roedern

12a. DISTRIBUTION/AVAILABILITY STATEMENT
National Technical Information Service
U.S. Department of Commerce
5285 Port Royal Road
Springfield, VA 22161

12b. DISTRIBUTION CODE

13. ABSTRACT *(Maximum 200 words):* The objectives of this project were to obtain a fundamental understanding of wide-gap chalcopyrite semiconductors and photovoltaic devices. Information to be gathered included significant new fundamental materials data necessary for accurate modeling of single- and tandem-junction devices, basic materials science of wider-gap chalcopyrite semiconductors to be used in next-generation devices, and practical information on the operation of devices incorporating these materials. Deposition used a hybrid sputtering and evaporation method shown previously to produce high-quality epitaxial layers of $Cu(In,Ga)Se_2$ (CIGS). Materials analysis was also provided to assist members of the National CIS Team, of which, through this contract, we were a member. Solar cells produced from resulting single-crystal epitaxial layers in collaboration with various members of the CIS Team were used to determine the factors limiting performance of the devices based on analysis of the results. Because epitaxial growth allows us to determine the surface orientation of our films specifically by choice of the substrate surface on which the film is grown, a major focus of the project concerned the nature of (110)-oriented CIGS films and the performance of solar cells produced from these films. We begin this summary with a description of the results for growth on (110) GaAs, which formed a basis for much of the work ultimately conducted under the program.

14. SUBJECT TERMS: PV; manufacturing; thin film; chalcopyrite semiconductor; hybrid sputtering; scanning electron microscopy; atomic force microscopy; energy dispersive X-ray spectroscopy; backscattering diffraction patterns; wide gap;

15. NUMBER OF PAGES

16. PRICE CODE

17. SECURITY CLASSIFICATION OF REPORT Unclassified	18. SECURITY CLASSIFICATION OF THIS PAGE Unclassified	19. SECURITY CLASSIFICATION OF ABSTRACT Unclassified	20. LIMITATION OF ABSTRACT UL